# Unravelling the Electromechanical Coupling in Graphene/bulk *h*-BN Heterostructure

Xingan Jiang[1#], Xiangping Zhang[1#], Xiangyan Han[2], Jianming Lu[2], Xueyun Wang[1*] and Jiawang Hong[1*]

[1]School of Aerospace Engineering, Beijing Institute of Technology, Beijing, 100081, China

[2]State Key Laboratory for Mesoscopic Physics and Frontiers Science Center for Nano-optoelectronics, School of Physics, Peking University, Beijing 100871, China

*Corresponding Authors Emails: xueyun@bit.edu.cn, hongjw@bit.edu.cn

[#]These authors contribute equally to this work

## Abstract

The stacking heterostructure of graphene on bulk *h*-BN produces a moiré pattern with topographic corrugation. The corrugation of the moiré pattern expectantly induces a considerable curvature and a flexoelectric response, which calls for detailed study. In this work, we used lateral force microscopy, a scanning technique to locally observe the moiré pattern and topographic corrugation. The curvature and flexoelectric potentials are derived from the measured topographic corrugation, revealing a huge curvature of ~$10^7$/m and a flexoelectric potential of ~10 mV in the hexagonal domain wall region (~3-4 nm) of the moiré pattern. In addition, the domain walls in moiré pattern also generate a clear electromechanical and frictional response, arising from the corrugation-induced flexoelectric response. In summary, the results of this work provide insights to understand the flexoelectricitiy in the Graphene/bulk *h*-BN and its associated electromechanical coupling behavior in the moiré pattern of van der Waals stacking heterostructure.

**Keywords:** Moiré pattern; Curvature; Flexoelectricity; Electromechanical coupling; Friction

## 1 Introduction

The stacking of two-dimensional (2D) van der Waals monolayers with slightly dissimilar lattice constants and/or small-angle twist produces a newly periodic structure known as moiré pattern, which emerges from multiple misaligned moiré lattices or inhomogeneous strain distributions[1,2]. Moiré pattern has given rise to a panoply of fascinating phenomena that the individual layer does not exhibit, such as superconductivity[3], exciton trapping[4], correlated insulator phases[5], novel magnetic ground state[6], and slide ferroelectricity[7].

The study of strain field in moiré pattern is a lively field[2,8,9]. Recently, the inhomogeneous strain in domain walls, i.e., strain gradient, are not only of particular interest, but their presence could also explain recent experiments where novel electromechanical coupling was discovered in moiré pattern due to a strong inhomogeneous strain[8,10,11]. For example, the inhomogeneous strain leads to energy gaps which are often interpreted in terms of large pseudomagnetic fields by bending graphene ribbons[11]. In twisted bilayer graphene, polarized domain walls were discovered in moiré pattern due to the in-plane strain gradient induced flexoelectric polarization[10]. It should be also noted that the topographic corrugation is also present in the moiré pattern due to the interfacial interaction between two stacking layers. The corrugation expectantly generates a considerable curvature and flexoelectric response, which calls for quantitative study. Graphene on hexagonal boron nitride (G/bulk *h*-BN) is one of the most interesting van der Waals heterostructures as the lattice constants only shows 1.8% difference. Ab initio calculations show that the interactions between graphene and *h*-BN are dominated by the C-N interaction[12]. Graphene deforms regularly on *h*-BN in the out-of-plane direction due to the asymmetry in C-N and C-B interactions and different stacking order in different region, forming a wavy corrugation with a period as that of moiré pattern[13].

In this work, we used a small tip-sample contact force (～8 nN) to facilitate the high-resolution imaging of moiré pattern by lateral force microscopy, a scanning technique with enhanced topographic features. The corrugation-induced curvature and flexoelectric potentials were further derived, which generates the out-of-plane electromechanical coupling and synergistically modulates the frictional behavior

experienced by the scanning tip. The corrugation-induced flexoelectric effect in moiré pattern also expectantly have more consequences to be explored for novel physical coupling phenomena in moiré pattern.

## 2 Experimental method

**The preparation of the Graphene/bulk *h*-BN heterostructure:** Graphene/bulk *h*-BN heterostructure was prepared by layer transfer technique. Firstly, bulk *h*-BN flake was exfoliated onto a PDMS/PPC stamp. Then the graphene flake on a $SiO_2$/Si substrate was picked up sequentially with bulk *h*-BN on PDMS. Subsequently, the graphene/bulk *h*-BN structure was flipped over and picked up with a PDMS/PMMA stamp and then transferred from the PMMA onto the silicon wafer to expose graphene on bulk *h*-BN.
**The characterization of the moiré pattern:** We performed lateral force microscopy (LFM) and piezoresponse force microscopy (PFM) by using a commercial atomic force microscope (Asylum Research MFP-3D) to locally measure the topographic corrugation and the electromechanical coupling. In PFM mode, the PFM signal was acquired at the drive frequency of 350 kHz and *ac* voltage ($V_{ac}$ = 0.5–1 V) with the Pt/Ir-coated Si cantilever tip (radius ~25 nm), the spring constants is ~2.8 N/m. In LFM measurement, using a small tip-sample contact force ~8 nN facilitates the high-resolution imaging of moiré pattern. The frictional signal was acquired at a relatively larger contact force of 24 nN. The details of tip force calibration are shown in **Supplementary Fig. 1**.

## 3 Results and discussion

### 3.1 The characterization of moiré pattern in Graphene/bulk *h*-BN heterostructure by lateral force microscopy scanning technique

The schematic for the lateral force microscopy (LFM) scanning characterization of G/bulk *h*-BN heterostructure is given in **Figure 1a**. **Figure 1b** shows the topographic image of G/bulk *h*-BN heterostructure stacked on polypropylene carbonate (PPC). **Figure 1c-d** show three main stacking configurations, namely AB stacking, BA stacking and AA stacking in G/bulk *h*-BN heterostructure, and the moiré pattern with perfectly alignment or small twist angle (0˚-1˚) [14]. AB regions (N atom stacks in the center of a graphene hexagon) have lowest energy stacking order and occupy the largest

area in the reconstructed structure. BA stacking (where a B atom stacks in the center of a graphene hexagon) was only slightly lower energy stacking order than the one of AA stacking (all atoms locating on top of other atoms). To image the moiré pattern in LFM mode, a sharp and soft probe are used for a higher resolution with a probe radius of ~10 nm and cantilever spring $k$ of ~0.29 N/m in our experiment. Using a small tip-sample contact force facilitates the high-resolution imaging of moiré pattern. The details of tip force calibration are shown in **Supplementary Fig. 1**. **Figure 1e** shows the topographic image of moiré pattern in G/bulk *h*-BN heterostructure measured using a very small contact force of 8 nN. The height profiles along the white line in moiré pattern shows a clear topographic corrugation with the height amplitude of ~40-50 pm, which is close to the theoretical values from DFT[13]. The moiré period ($\lambda$) from the fast Fourier transform in the inset as well as the height profile along the white line is determined to be around 15.05 nm, close to the perfectly aligned graphene on bulk *h*-BN.

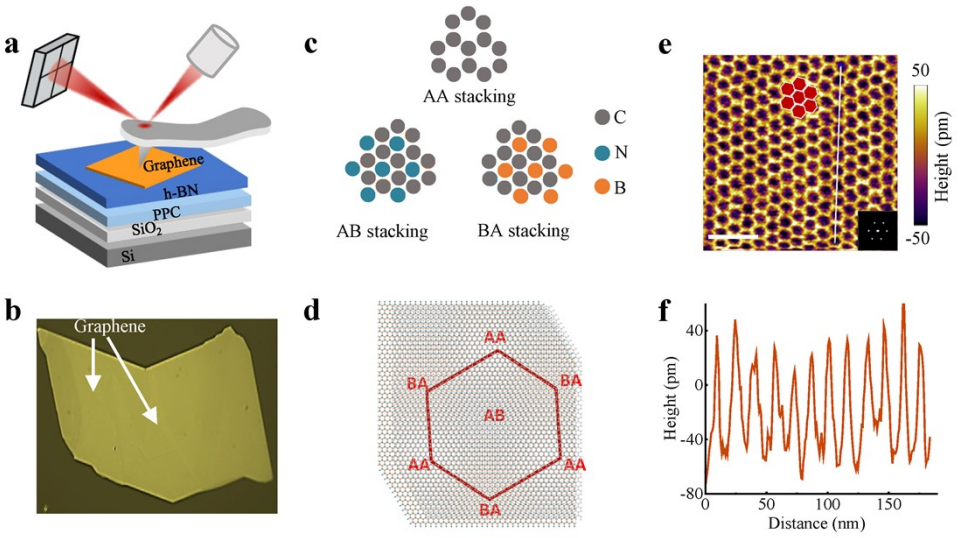


**Figure 1. Schematic diagram for characterization on Graphene/ bulk *h*-BN (G/bulk *h*-BN) moiré pattern by lateral force microscopy. a** The topographic signal is detected by the quadrant photodetector during the probe scanning over the G/bulk *h*-BN/PPC/$SiO_2$/Si sample. **b** The topographic image of graphene/*h*-BN heterostructure stacked on PPC. **c** The three main stacking configurations: AB stacking (N atom sits in the center of a graphene hexagon), BA stacking (B atom sits in the center of a graphene hexagon) and AA stacking (all atoms sitting on top of other atoms) in G/bulk *h*-BN heterostructure, and **d** their locations in moiré pattern with perfectly alignment or small twist angle (0°-1°). **e** The periodic topographic corrugation of moiré pattern in G/bulk *h*-BN heterostructure, and the inset is fast Fourier transform (FFT). **f** The height profiles across the white line in moiré pattern of **Figure 1e** shows a clear topographic corrugation. The scale bar is 40 nm.

### 3.2 The curvature and flexoelectric potential analysis in the G/bulk *h*-BN moiré pattern

The topographic corrugation in the moiré pattern expectantly induces a considerable curvature. The curvature is introduced to describe the flexoelectricity in G/bulk *h*-BN stacking heterostructure, similar to the case in buckling graphene[15]. **Figure 2a** shows the topography of moiré pattern with a different period ($\lambda$) of ~15.05 nm, 11.82 nm and 9.51 nm, respectively. The ratio $d/\lambda$ is evaluated to be 0.22, 0.23 and 0.25, revealing a high commensurate state[1]. The details of the estimated $d/\lambda$ on the entire topographic images are shown in **Supplementary Fig. 2.** It is noted that the topography profile is regarded as a superimposed effect of deformations in stacking layers. The deflection ($w$) and curvature ($\kappa_i$) of the heterostructure has the following relationship[16]:

$$\kappa_x = -\frac{\partial^2 w}{\partial x^2}, \quad \kappa_y = -\frac{\partial^2 w}{\partial y^2} \qquad \text{* MERGEFORMAT (1)}$$

Herein, the Cartesian coordinate system ($x$, $y$) is used to calculate the curvature in moiré pattern. **Figure 2b**-**2c** shows the calculated curvature $\kappa_x$ and $\kappa_y$ in the $x$ and $y$ direction, respectively. A clear contrast in curvature exists between domains (AB stacking) and domain walls (BA, AA stacking), and the curvature in domain walls region reaches $10^7$ $m^{-1}$. It should be noted that the choice of axes orientation in the strain gradient calculation yields negligible difference in the magnitude of strain gradient, as shown in **Supplementary Fig. 3.** We further calculated the curvature-induced flexoelectric surface potentials. According to the flexoelectric constitutive equation[17–19], the flexoelectric field can be calculated by the flexoelectric coupling coefficient $f_{zx}$,$f_{zy}$ and the curvature $\kappa_x$,$\kappa_y$ according to the relation:

$$E_z = f_{zx}\kappa_x + f_{zy}\kappa_y \qquad \text{* MERGEFORMAT (2)}$$

Here we consider the flexoelectric coupling coefficient $f_{zx}$,$f_{zy}$ as a constant value $f$. $f$ can be obtained by the flexoelectric coefficient $\mu$ and permittivity $\varepsilon$ according to the relation of $f = \mu\varepsilon^{-1}$[20,21]. The values of $\mu$ and $\varepsilon$ of graphene are -0.03 nC/m and $39.8\times10^{-12}$ F/m, respectively[22–24]. The surface potential can be obtained by integrating the flexoelectric field:

$$V_{surface}(x,y) = \int_0^{\infty} E_z(x,y,z)dz \qquad \text{* MERGEFORMAT (3)}$$

**Figure 2d** shows the distribution of the calculated flexoelectric potentials in moiré pattern with a varied period. A clear hexagonal distribution of potentials was observed in moiré pattern. The domain walls with high potentials (~10 mV) can be clearly distinguished from domains with low potentials.

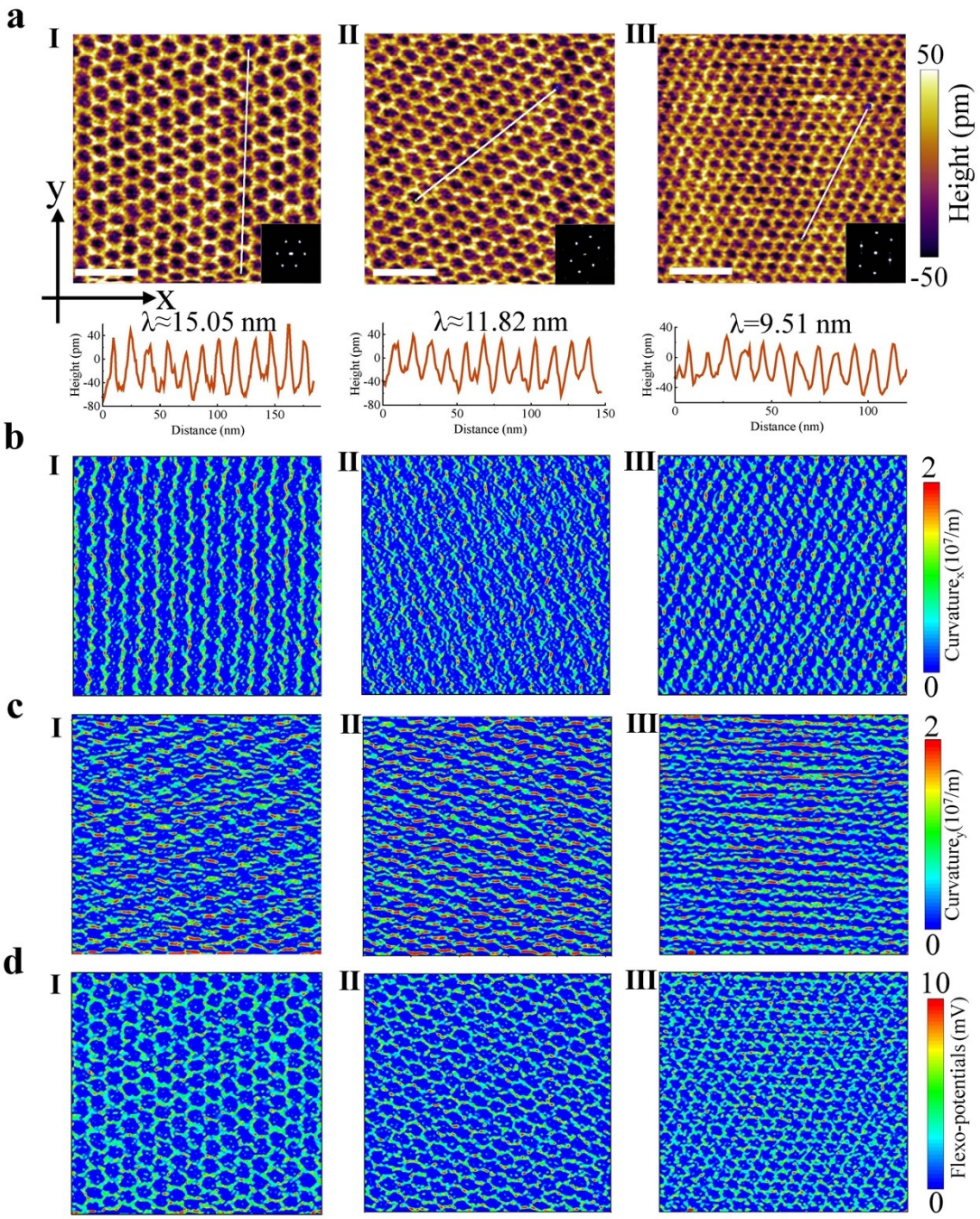


**Figure 2. The curvature and flexoelectric potential analysis in the G/bulk *h*-BN moiré pattern.** **a** The topographic images with height profiles and fast Fourier transform (FFT). **b** and **c** The curvatures along the *x* and *y* directions, respectively. **d** The distribution of flexoelectric potentials in moiré patterns. The scale bar is 50 nm.

### 3.3 The piezoresponse induced by the flexoelectricity in G/bulk *h*-BN moiré pattern

The flexoelectric polarization can give rise to a mechanical response to the external electric field, which can be detected by piezoresponse force microscopy (PFM)[8]. Therefore, PFM measurements were conducted on a large area of G/bulk *h*-BN moiré pattern. However, the intrinsic PFM signal is highly interfered by the background signal, which leads to the vague phase contrast[10]. As shown in **Figure 3a**, the intrinsic phase signal can be revealed with a phase contrast close to 90˚ by deducting the noise vector. **Figure 3b-3d** show the topography, phase and amplitude in moiré pattern after deducting the noise vector, respectively. The original PFM image was shown in **Supplementary Fig. 4**. The domain walls exhibit a phase contrast close to 90° and a strong piezoresponse compared to the domain region. Moreover, the topography is not responsible for the PFM contrast, which is revealed by a comparative PFM scanning of G/bulk *h*-BN on uneven surface (**Supplementary Fig. 5**). These results imply the flexoelectricity as the origin to explain the results of piezoresponse signal.

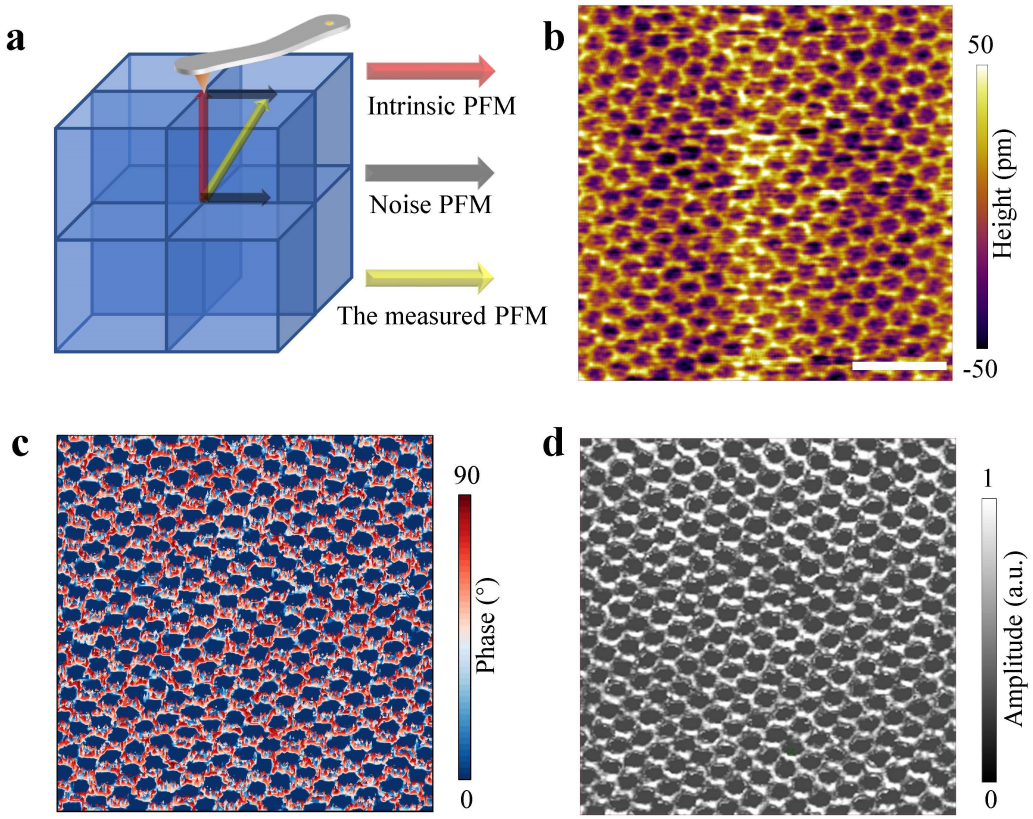


**Figure 3. The intrinsic PFM signal obtained by deducting the background noise. a** The PFM

noise signal leads to a low phase contrast. **b-d** The topographic corrugation, intrinsic phase and amplitude in moiré pattern, respectively. The scale bar is 50 nm.

### 3.4 The frictional modulation induced by the corrugation on G/bulk *h*-BN moiré pattern

We also would like to note that moiré pattern can be also readily visualized by friction behavior with exceptional high sensitivity and spatial resolution. The topographic and frictional maps in moiré pattern are measured using probes with different radius. The probe with a radius of ~10 nm gives a better resolution of the moiré pattern, as shown in **Figure 4a, b**. The domains with low friction are separated by domain walls with high friction. When the probe has a larger radius of ~100 nm, moiré pattern cannot be imaged by the topography measurement, but friction mode distinguishes the moiré pattern, as shown in **Figure 4c, d**. Moreover, the friction force mapping with different periodicities were also measured and shown in **supplementary Fig. 6**.

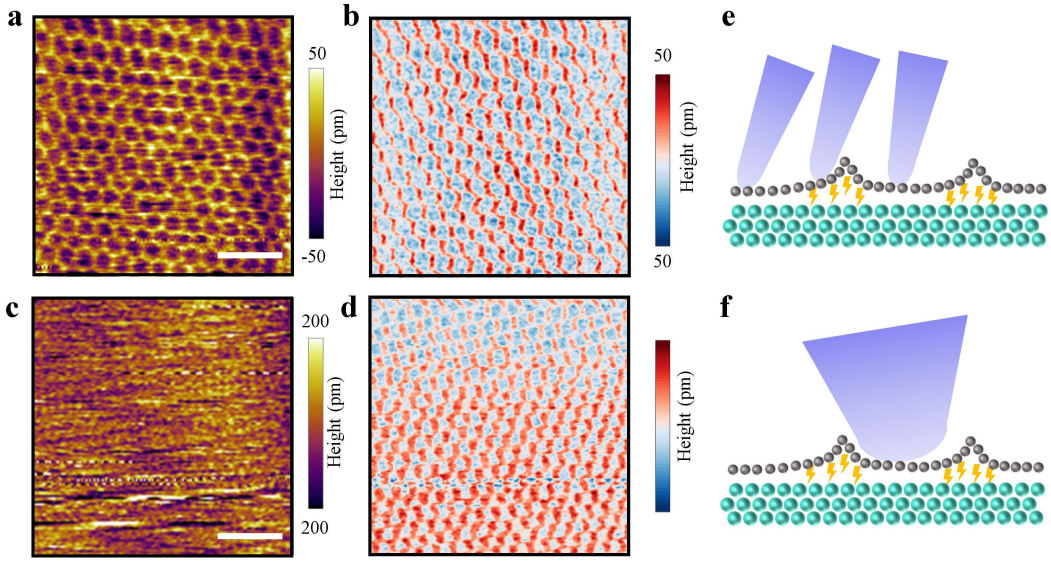


**Figure 4. The topographic and frictional map measured in moiré pattern using probes with different radius.** The topographic and frictional map measured using a soft probe with a radius ~10 nm **in a, b** and a radius ~100 nm in **c, d**, respectively. **e, f** The schematic diagram for the synergetic modulation of frictional behaviors by the topography and the flexoelectric potentials. The scale bar is 50 nm.

These results strengthen the fact that the frictional behavior in moiré pattern can be regulated by some other factors rather than purely from the topographic crosstalk. Herein, we believe that the curvature contributes partly to the modulation of friction

during the probe scanning on the moiré pattern. According to the Prandtl−Tomlinson model, the motion of AFM probe on graphene can be simplified to the motion of a point mass being dragged over a periodic potential by a supporting body through a spring[26]. The total potential energy of the system can be approximately expressed as

$$\mathrm{U}\left(x_p, x_s\right) = -\frac{U_L + U_M}{2}\cos\left(\frac{2\pi x_p}{a}\right) + \frac{k}{2}\left(x_p - x_s\right)^2 \quad (5)$$

where $U_L$ and $U_M$ are two-dimensional hexagonal potentials with the periodicity of the graphene lattice and of a moiré pattern, $x_p$ is the displacement of the point mass, $x_s$ is the displacement of the supporting body, $a$ is the lattice constant, and $k$ is the effective spring constant. The sharp domain walls exist with huge curvature, which creates a flexoelectric surface potential corrugation in periodic moiré pattern and expectantly modifies the friction behavior experienced by the probe.

## 4 Conclusions

In summary, we measured the topographic corrugation by lateral force microscopy and studied the flexoelectric effect in the graphene/bulk *h*-BN moiré pattern with a varied periodicities. The curvature and flexoelectric potentials are derived from the topographic corrugation, revealing a huge curvature of ~$10^7$ $m^{-1}$ value and flexoelectric potential of ~10 mV in the narrow domain walls region (~3-4 nm) in the moiré pattern. In addition, it was also experimentally found that the flexoelectrictiy in moiré pattern generates the electromechanical response and synergistically modulates the frictional behavior experienced by the scanning probe. Our findings stress the existence of topographic corrugation-induced flexoelectric potentials in moiré pattern and possibly have more consequences to be explored for the physical coupling phenomena in moiré pattern, which remains an open problem.

## Conflicts of interest

There are no conflicts of interest to declare

**Acknowledgements**

J.W.H. and X.Y.W. acknowledge the support by the Beijing Natural Science Foundation (Z190011) and the Beijing Institute of Technology Research Fund Program for Young Scholars. X.Y.W. acknowledges the support by National Key Research and Development Program of China (2019YFA0307900), and the National Natural Science Foundation of China (92163101). J.W.H. acknowledges the support by National Natural Science Foundation of China (12172047). X.A.J. acknowledges the support by National Natural Science Foundation of China (12202056).

**Author Contributions**

X.A. Jiang, X.P. Zhang contributed equally to this work. X.A. Jiang carried out the scanning probe measurements, X.P. Zhang performed the quantitative characterization on flexoelectric effect. X.Y. Han and J.M. Lu prepared the sample. X. Y. Wang and J. W. Hong conceived and supervised the project. All authors discussed and wrote the manuscript.

**Data Availability**

The data that support the findings of this study are available from the corresponding author on request.

**References**

1 C. R. Woods, F. Withers, M. J. Zhu, Y. Cao, G. Yu, A. Kozikov, M. Ben Shalom, S. V. Morozov, M. M. van Wijk, A. Fasolino, M. I. Katsnelson, K. Watanabe, T. Taniguchi, A. K. Geim, A. Mishchenko and K. S. Novoselov, *Nat Commun*, 2016, **7**, 10800.

2 C. R. Woods, L. Britnell, A. Eckmann, R. S. Ma, J. C. Lu, H. M. Guo, X. Lin, G. L. Yu, Y. Cao, R. V. Gorbachev, A. V. Kretinin, J. Park, L. A. Ponomarenko, M. I. Katsnelson, Yu. N. Gornostyrev, K. Watanabe, T. Taniguchi, C. Casiraghi, H.-J. Gao, A. K. Geim and K. S. Novoselov, *Nature Phys*, 2014, **10**, 451–456.

3 Y. Cao, V. Fatemi, S. Fang, K. Watanabe, T. Taniguchi, E. Kaxiras and P. Jarillo-

Herrero, *Nature*, 2018, **556**, 43–50.

4 K. L. Seyler, P. Rivera, H. Yu, N. P. Wilson, E. L. Ray, D. G. Mandrus, J. Yan, W. Yao and X. Xu, *Nature*, 2019, **567**, 66–70.

5 Y. Cao, V. Fatemi, A. Demir, S. Fang, S. L. Tomarken, J. Y. Luo, J. D. Sanchez-Yamagishi, K. Watanabe, T. Taniguchi, E. Kaxiras, R. C. Ashoori and P. Jarillo-Herrero, *Nature*, 2018, **556**, 80–84.

6 K. S. Burch, D. Mandrus and J.-G. Park, *Nature*, 2018, **563**, 47–52.

7 M. Vizner Stern, Y. Waschitz, W. Cao, I. Nevo, K. Watanabe, T. Taniguchi, E. Sela, M. Urbakh, O. Hod and M. Ben Shalom, *Science*, 2021, **372**, 1462–1466.

8 L. J. McGilly, A. Kerelsky, N. R. Finney, K. Shapovalov, E.-M. Shih, A. Ghiotto, Y. Zeng, S. L. Moore, W. Wu, Y. Bai, K. Watanabe, T. Taniguchi, M. Stengel, L. Zhou, J. Hone, X. Zhu, D. N. Basov, C. Dean, C. E. Dreyer and A. N. Pasupathy, *Nat. Nanotechnol.*, 2020, **15**, 580–584.

9 N. P. Kazmierczak, M. Van Winkle, C. Ophus, K. C. Bustillo, S. Carr, H. G. Brown, J. Ciston, T. Taniguchi, K. Watanabe and D. K. Bediako, *Nat. Mater.*, 2021, **20**, 956–963.

10 Y. Li, X. Wang, D. Tang, X. Wang, K. Watanabe, T. Taniguchi, D. R. Gamelin, D. H. Cobden, M. Yankowitz, X. Xu and J. Li, *Advanced Materials*, 2021, **33**, 2105879.

11 F. Guinea, A. K. Geim, M. I. Katsnelson and K. S. Novoselov, *Phys. Rev. B*, 2010, **81**, 035408.

12 M. Bokdam, T. Amlaki, G. Brocks, P. J. Kelly, Physical review, B. Condensed matter and materials physics, 2014, 89: 201404.

13 M. M. Van Wijk, A. Schuring, M. I. Katsnelson and A. Fasolino, Physical Review Letters, 2014, 113(13): 135504-135504.

14 N. Y. Kim, H. Y. Jeong, J. H. Kim, G. Kim, H. S. Shin, and Z. Lee, Acs Nano, 2017, 11 (7): 7084–7090.

15 T. Dumitrică, C. M. Landis and B. I. Yakobson, *Chemical Physics Letters*, 2002, **360**: 182–188.

16 M. Springolo, M. Royo, and M. Stengel, Physical review letters, 2021, **127**(21):

216801.

17 C. A. Mizzi, A. Y. W. Lin and L. D. Marks, *Phys. Rev. Lett.*, 2019, **123**, 116103.

18 S. Huang, L. Qi, W. Huang, L. Shu, S. Zhou and X. Jiang, *J. Adv. Dielect.*, 2018, **08**, 1830002.

19 X. Jiang, X. Wang, X. Wang, X. Zhang, R. Niu, J. Deng, S. Xu, Y. Lun, Y. Liu, T. Xia, J. Lu and J. Hong, *Nat Commun*, 2022, **13**, 574.

20 P. Zubko, G. Catalan and A. K. Tagantsev, *Annu. Rev. Mater. Res.*, 2013, **43**, 387–421.

21 B. Wang, Y. Gu, S. Zhang and L.-Q. Chen, *Progress in Materials Science*, 2019, **106**, 100570.

22 J. Hong and D. Vanderbilt, *Phys. Rev. B*, 2013, **88**, 174107.

23 E. J. G. Santos and E. Kaxiras, *Nano Lett.*, 2013, **13**, 898–902.

24 L. J. McGilly, A. Kerelsky, N. R. Finney, K. Shapovalov, E. M. Shih, A. Ghiotto, ... and A. N. Pasupathy, Nature Nanotechnology, 2020, **15**(7), 580-584.

25 A. Davies, J. D. Albar, A. Summerfield, J. C. Thomas, T. S. Cheng, V. V. Korolkov, E. Stapleton, J. Wrigley, N. L. Goodey, C. J. Mellor, A. N. Khlobystov, K. Watanabe, T. Taniguchi, C. T. Foxon, L. Eaves, S. V. Novikov and P. H. Beton, *Nano Lett.*, 2018, **18**, 498–504.

26 S. Zhang, T. Ma, A. Erdemir and Q. Li, *Materials Today*, 2019, **26**, 67–86.